Electronic, vibrational, Raman, and scanning tunneling microscopy signatures of two-dimensional boron nanomaterials

Daniel V. P. Massote,[1,2] Liangbo Liang,[1,3] Neerav Kharche,[1] and Vincent Meunier[1,*]

[1]*Department of Physics, Astronomy, and Applied Physics, Rensselaer Polytechnic Institute, Troy, New York 12180, USA*

[2]*Departamento de Fsica, ICE, Universidade Federal de Juiz de Fora, Juiz de Fora, Minas Gerais, 36036-900, Brazil*

[3]*Center for Nanophase Materials Sciences, Oak Ridge National Laboratory, Oak Ridge, Tennessee 37831, USA*

(Received 20 May 2016; revised manuscript received 3 October 2016; published 11 November 2016)

Compared to graphene, the synthesis of large area atomically thin boron materials is particularly challenging, owing to the electronic shell structure of B, which does not lend itself to the straightforward assembly of pure B materials. This difficulty is evidenced by the fact that the first synthesis of a pure two-dimensional boron was only very recently reported, using silver as a growing substrate. In addition to experimentally observed 2D boron allotropes, a number of other stable and metastable 2D boron materials are predicted to exist, depending on growth conditions and the use of a substrate during growth. This first-principles study based on density functional theory aims at providing guidelines for the identification of these materials. To this end, this report presents a comparative description of a number of possible 2D B allotropes. Electronic band structures, phonon dispersion curves, Raman scattering spectra, and scanning tunneling microscopy images are simulated to highlight the differences between five distinct realizations of these B systems. The study demonstrates the existence of clear experimental signatures that constitute a solid basis for the unambiguous experimental identification of layered B materials.

DOI: 10.1103/PhysRevB.94.195416

I. INTRODUCTION

Following the seminal report of graphene's discovery in 2004 [1], the study of two-dimensional (2D) materials has attracted intense interest, due to their promise for electronic and optoelectronic applications. The unique properties of these materials have prompted much attention, and great effort in understanding and modifying the structure of 2D materials has been pursued. These developments also opened up a new research era for the discovery of other atomically thin materials with attractive properties for potential applications. As a result, in addition to steady progress made in understanding graphene, h-BN, and transition metal dichalcogenides [2], other monoelemental layered materials have been investigated, including silicene [3–6], germanene [7–9], stanene [10], and phosphorene [11–14]. One of the latest systems to have been experimentally realized is 2D boron material, as reported by two independent groups since 2015 [15–17]. Unlike most other systems studied thus far, boron cannot be obtained by exfoliation techniques since it does not possess a stable 3D crystalline form, let alone a layered one. While boron, when associated with nitrogen, readily forms atomically flat semiconducting layered materials (i.e., h-BN), in its monoelemental form, boron has proven much more complicated to assemble into 2D systems. However, the recent discoveries by Mannix *et al.* and Feng *et al.* have demonstrated the possibility of developing pure boron-based 2D materials, thereby opening up new potential opportunities for the development of boron-based nanotechnology [15,16].

With nitrogen, boron is the closest element to carbon in the periodic table, and like carbon, its assembly in 2D systems would result in lightweight materials with properties stemming from the 2D quantum confinement of its electrons within one plane. However, compared to carbon, boron features one less electron in its outer shell and is therefore not able to form bonds in the way carbon develops sp^2 bonding. The quest to understanding boron properties has been evidenced by a number of theoretical and numerical studies. For instance, Tang *et al.* proposed a scheme in which boron could be stabilized in flat sheets in such a way that the hexagonal lattice features atoms at the center of some hexagonal holes while others are kept empty [Fig. 1(c)] [18,19]. The mechanism behind this material's stability is based on the so-called 3*c*-2*e* (i.e., three center two electrons) bond stabilization that satisfies the Aufbau principle for boron (i.e., electrons are shared in such a way as to optimize low-energy level occupancies). Tang *et al.* also determined the amount of holes in the structure that provides the lowest energy. For example, these authors predicted α-sheet to be the most stable system among a series of investigated structures. α-sheet material shows remarkable structural simplicity and was determined to be metallic, according to density functional theory (DFT) calculations performed within a generalized gradient approximation (GGA).

Following the investigation of boron α-sheet, a number of studies highlighted different and possible lowest energy candidates to accommodate boron atoms on a single, atomically-thin 2D system. Among these, Wu *et al.* identified a number of metastable candidates for the boron sheet, in addition to the α-sheet studied before [20]. The overall structural stability of the α-sheet was examined by calculating phonon dispersion curve, which features a soft mode at the high symmetry *M* point of the hexagonal Brillouin zone. This mode indicates that atoms at the center of hexagons should be puckered upward and downward in the sheet plane to accommodate this structural instability. Note that the α-sheet is renamed α'-sheet when the atoms are puckered. In addition, using the PBE0 hybrid functional, the authors of this study showed that this material is a semiconductor featuring a 1.1 eV band gap.

*meuniv@rpi.edu

To determine the most stable 2D boron system among a set of possible structures, Zhou *et al.* used an evolutionary algorithm search and identified two new possible phases for boron sheets [21]. Both structures are characterized by eight atoms in their unit cell and belong to the *Pmmm* and *Pmmn* space groups, respectively. Both systems are metallic and the *Pmmn* allotrope has a distorted Dirac cone near the Fermi energy. It was determined that these two systems are 80 and 50 meV/atom more stable than the α'-sheet. It is worth noting that the *Pmmm* boron sheet is not an exactly flat single-layer material as it features an approximately 4 Å corrugation.

In a related study, Zhang *et al.* investigated how the presence of a substrate (such as silver, gold, nickel, or copper) affects the stability of 2D boron [22]. These authors predicted that the interaction between boron and a metal affects significantly the possible stable and metastable structures that emerge from the algorithmic search. Since boron materials are likely to have high degeneracy regarding defect energies [23], the presence of a metallic substrate might down-select probable structures in the computational search. In particular, the numerical search yielded one particularly simple structure named boron 1/6-sheet that was predicted to be the most stable in the presence of a copper or nickel substrate.

Experiments performed by Mannix *et al.* confirm that substrate interaction is a key feature determining the details of boron material synthesis [15]. They performed epitaxy experiments along with DFT calculations to verify whether the observed material could be found using evolutionary algorithms. The synthesized material, known as *borophene*, has a *Pmmn* symmetry and planar lattice constants of 0.500 nm and 0.289 nm. The structure is commensurate with the lattice of the silver substrate, and depending on the experimental conditions, a pattern of stripes can be observed by scanning tunneling microscopy (STM). These authors also observed some structural distortion, as a result of the interaction between boron and the silver substrate. Surface characterization such as Auger spectroscopy, XPS, and STM confirmed the experimental observations and the theoretical predictions.

Shortly following the first observation, Feng *et al.* reported the synthesis of a second type of 2D boron materials by molecular beam epitaxy (MBE) experiments on silver substrates [16,17]. They reported the synthesis of boron 1/6-sheet (also named β_{12}) and another phase called χ_3. The samples were characterized by STM, XPS, as well as DFT calculations. In a follow-up work, Feng *et al.* also characterized boron 1/6-sheet as a metallic system [17].

These experiments constitute an important milestone in the search for 2D boron materials. However, they leave open the possibility to find other stable structures, especially since the technical difficulty to synthesize the materials yield the creation of a number of metastable structure, depending on experimental conditions, including the use of a specific substrate during synthesis. To assist in the quest of characterizing these and other 2D boron materials, we performed a set of first-principles calculations including structural, electronic, and accurate phonon dispersion calculations to develop a catalog of properties using a unified computational and theoretical framework. These calculations allow us to compute Raman scattering and STM images of *Pmmm*, *Pmmn*, α'-sheet, 1/6-sheet, and borophene layers. Our results show that most materials have clearly different Raman spectra and STM signatures, making it easy to discern a clear difference between the various possible structural phases.

II. METHODS

Unless otherwise stated, all calculations presented here were performed within the DFT [24] framework as implemented in the VASP code [25,26]. We made use of the PAW [27] method and employed the PBE functional for the exchange-correlation interaction [28]. For the sole semiconducting system, α'-sheet, we also employed the hybrid PBE0 functional to obtain a more accurate estimate of the electronic band gap [29]. All structures were relaxed down to 10^{-4} eV/Å with a plane-wave basis set of 400 eV. Vacuum space between images was at least 10 Å in the direction perpendicular to the boron sheets. In all calculations, the 2D materials were oriented in the xy plane with z chosen as the nonperiodic direction. Brillouin-zone sampling was determined so that the total energies were numerically converged. Turning to characterization, the simulated scanning tunneling microscopy images were computed using converged electronic densities within the Tersoff-Hamann approximation [30].

We computed the phonon spectrum of each structure and then calculated nonresonant first order Raman scattering with fully relaxed geometries. The Raman intensity of the jth phonon mode is obtained by [31–33]

$$\frac{d\sigma}{d\Omega} = N_{\text{prim}} \frac{\omega_s^4}{c^4 V_{\text{prim}}} |\mathbf{g}_s \cdot \tilde{\boldsymbol{R}}(j) \cdot \mathbf{g}_i^T|^2 \times \frac{\hbar}{2\omega_j}(n_j + 1), \quad (1)$$

where ω_i and ω_s are the frequencies of incoming and scattered lights, respectively. ω_j is the frequency of the jth phonon mode of the crystal. Energy conservation implies that $\omega_s = \omega_i \mp \omega_j$, where the negative (positive) sign describes the Stokes (anti-Stokes) process. V_{prim} is the volume of the primitive unit cell, N_{prim} is the number of primitive unit cells in the simulation domain, and c is the speed of light. The Bose factor of the jth phonon is $n_j = (e^{\hbar\omega/k_B T} - 1)^{-1}$. $\mathbf{g}_i$ and $\mathbf{g}_s$ are electric polarization vectors for incoming and scattered lights, respectively. The Raman susceptibility $\tilde{\boldsymbol{R}}(j)$ is a symmetric 3×3 tensor associated to the jth phonon mode. It can be calculated as [31,32,34]

$$\tilde{\boldsymbol{R}}_{\alpha\beta}(j) = V_{\text{prim}} \sum_{\mu=1}^{N} \sum_{l=1}^{3} \frac{\partial \chi_{\alpha\beta}}{\partial r_l(\mu)} \frac{e_l^j(\mu)}{\sqrt{M_\mu}}, \quad (2)$$

where $\chi_{\alpha\beta} = (\varepsilon_{\alpha\beta} - \delta_{\alpha\beta})/4\pi$ is the electric polarizability tensor related to the dielectric tensor $\varepsilon_{\alpha\beta}$. $r_l(\mu)$ is the position of the μth atom along direction l and $\frac{\partial \chi_{\alpha\beta}}{\partial r_l(\mu)}$ is the first derivative of the polarizability tensor with respect to the atomic displacement. $e_l^j(\mu)$ is the displacement of the μth atom along direction l in the jth phonon mode, and M_μ is the atomic mass of atom μ. Note that e^j and ω_j are eigenvectors and eigenvalues of dynamic matrix in the Brillouin zone center [32]. To calculate Raman scattering intensity from equations (1) and (2), one first needs to obtain the dynamic matrix and derivatives of dielectric tensor. The dynamic matrix is calculated using the direct method within DFT [35]

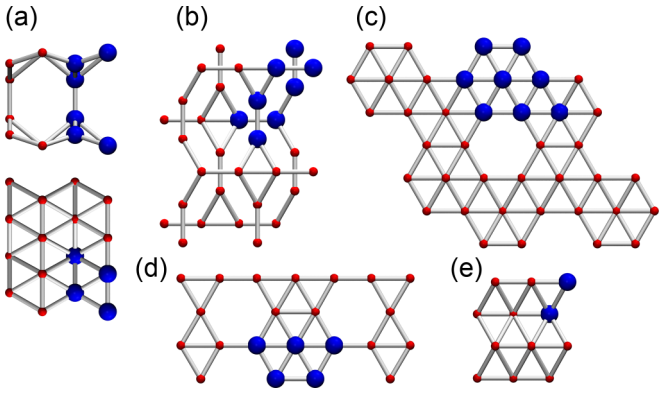

FIG. 1. Two-dimensional boron materials investigated in this study (top view). (a) *Pmmm* boron [also shown along the (010) direction], (b) *Pmmn* boron, (c) α'-sheet, (d) 1/6-sheet, and (e) borophene. The large spheres represent the atoms belonging to the primitive unit cell.

as implemented in the PHONON software [33]. In the finite difference scheme [36,37], Hellmann-Feynman forces in the supercell are calculated within VASP for both positive and negative displacements. These forces are then used in PHONON to construct the dynamic matrix. Once diagonalized, this matrix provides the frequencies ω_j and eigenvectors e^j of all $3N$ normal modes, where N is the number of atoms per unit cell. The dielectric tensor derivatives are also performed using finite differences in DFT. Since most of the materials under investigation are metallic, the frequency-dependent dielectric tensor was evaluated at 1.96 eV (633 nm) laser line, a commonly used frequency. More importantly, using the dynamic dielectric tensor at the laser frequency is physically correct in the Placzek approximation as reported in the literature [38–41], since it is the material's response at the frequency of the laser excitation that is relevant. Furthermore, by using the laser frequency-dependent dielectric tensor to calculate Raman intensities, resonant Raman effects can be also captured [39,41]. The Raman intensity for every phonon mode was obtained using backscattering setup. We choose polarization vectors ($\mathbf{g}_i$ and $\mathbf{g}_s$) parallel to the surface. All the spectra shown here are plotted after uniform Gaussian broadening.

III. RESULTS AND DISCUSSION

A. Structural properties

We start our discussion with the elementary properties of all structures mentioned above, as summarized in Table I for information related to lattice properties and relative structural energy. All structures were optimized in free-standing form, i.e., in the absence of a substrate.

The atomic structure of each investigated boron allotrope is shown in Fig. 1. The fully optimized coordinates for nonequivalent atoms are provided in the Supplemental Material (SM) [42]. Boron *Pmmm* and *Pmmn* are depicted in Figs. 1(a) and 1(b). These two systems feature out-of-plane corrugations greater than 0.5 Å. The α'-sheet [Fig. 1(c)] consists of a trigonal lattice with eight atoms in the unit cell. The ninth atom that would be present in a 3×3 lattice is removed, corresponding to a hole density $\eta = 1/9$, as defined by Tang *et al.* [18,19]. The proposed structure of Zhang *et al.* and later synthesized by Feng *et al.*, [16,22] boron 1/6-sheet [Fig. 1(d)], is also composed of five atoms and one hole per unit cell. This material belongs to the space group *Pmmn*, and its lattice parameters agree very well with experiments. In a recent study of synthesis of boron, Zhang *et al.* concluded that 1/6-sheet is capable of accommodating ripples present on silver substrates due to its smaller bending stiffness as compared to other 2D materials, such as graphene and h-BN [43]. Notably, borophene [Fig. 1(e)] has the same symmetry but its unit cell only contains two atoms, if we do not consider surface puckering. In this case, the unit cell is relatively small, yielding lattice parameters $L_x = 1.61$ and $L_y = 2.87$ Å. Experimental study found a larger 3×1 unit cell which maps, due to the commensurability with the underlying substrate.

Our calculations indicate that with the notable exception of the α'-sheet, all boron materials studied here display a metallic behavior, in agreement with previous calculations and experiments (see SM) [17,42]. Since it features a band gap, the geometry and band structure of the α'-sheet were studied with both PBE and PBE0 functionals (since PBE0, which includes a portion of exact exchange interaction, is known to yield a more accurate band gap value). We find small differences in the geometry (less than 1%) between the structures obtained using the semilocal and nonlocal exchange-correlation functional calculations, and the band structure shows a shift of states near the Fermi level, with a resulting opening of the band gap for PBE0, as already reported by Wu *et al.* [20]. Likewise, to calculate Raman spectra and STM images of the α'-sheet, we employed the PBE0 hybrid functional since it represents electronic properties more accurately than PBE.

B. Vibrational properties and Raman signatures

The phonon dispersion for all boron phases is plotted in Fig. 2. We note that phonon dispersions of both boron *Pmmm* and *Pmmn* in Fig. 2 are quite distinct from the results shown in an earlier work [21]. To clarify the issue, we carefully checked our results using the QUANTUM ESPRESSO code [44] and calculated the phonon dispersions of *Pmmm* and *Pmmn* polymorphs using density functional perturbation theory with the same computational protocol used by Zhou *et al.* [21]. These tests confirm that the spectra shown here accurately represent the phonon dispersion of the material. To assess the structural stability of the α'-sheet, we calculated the full phonon dispersion with PBE functional (Fig. 2) while only Γ point phonon modes were calculated within PBE0 due to computationally expensive calculations.

We also note that the recently synthesized borophene shows no negative frequency in the Brillouin zone in its freestanding form (Fig. 2), as opposed to results shown in earlier work [15]. This indicates that the structure does not have intrinsic structural instabilities, even in the free-standing geometry considered here. We should emphasize that a large 14×14 supercell was needed to obtain converged phonons with no negative frequency, indicating the nonlocal effect associated with local changes in the B-B interaction. This also confirms that much care is needed to evaluate phonon frequencies numerically. In fact, when a smaller supercell

TABLE I. Symmetry, optimized lattice parameters, total energy per atom, and relative energy differences between different phases considered in this work and shown in Fig. 1.

Phase	Space group	Point group	L_x(Å)	L_y(Å)	γ(°)	Energy/atom (eV)	Δ (meV)
Pmmm	*Pmmm* (47)	D_{2h}	2.88	3.25	90	−6.355	0
Pmmn	*Pmmn* (59)	D_{2h}	3.26	4.52	90	−6.327	28
α'-sheet	$P\bar{3}m1$ (164)	D_{3d}	5.03		120	−6.284	71
1/6-sheet	*Pmmn* (59)	D_{2h}	2.94	5.04	90	−5.192	1163
borophene	*Pmmn* (59)	D_{2h}	1.61	2.87	90	−6.185	170

was used, we reproduced the same cuspid-shaped mode near the *X* point in the phonon dispersion reported before [15]. Mannix *et al.* argue that long wavelengths are responsible for this effect [15]. which could account for the need of an increasing cell size. We also note that puckering introduced by the silver substrate, and measured by Mannix *et al.* [15], does not significantly affect borophene's phonon dispersion. Apart from the supercell size issue mentioned above, our unperturbed calculation is in good agreement with Mannix's simulations, which confirms that silver substrate interaction has small influence on phonon dispersion. Further, borophene is determined to be stable even in the absence of a substrate, even if a substrate is needed in the current synthesis process.

Similar to borophene, boron 1/6-sheet, which was also synthesized [16], does not present negative phonon frequencies and is a completely flat material. As discussed for the case of borophene, though a substrate is necessary for synthesis, it is not necessary for intrinsic stability. In contrast with borophene, we note that boron 1/6-sheet does not need the use of a very large supercell to avoid imaginary frequencies.

The knowledge of all phonon modes is not sufficient to assess Raman signals since the modes must correspond to a net change in polarizability to be active [selection rule, Eq. (2)]. In addition, this selection rule can yield signal with very low Raman intensity even for symmetry-allowed Raman modes. Some peaks can even disappear from the spectra, according to Eq. (1), for specific polarizations of the incoming and outgoing radiations. The present analysis enables the determination of which modes can potentially be observed for all structures considered. The spectra shown in Fig. 3 correspond to a backscattering condition as mentioned in the Methods section. Table II provides all symmetries and frequencies of calculated modes, and all the modes are visualized with a ball-and-stick and arrows representation in the SM [42]. As a trend, we observe that lower frequency modes below 1000 cm^{-1} are related to out-of-plane vibrations while the high frequency modes correspond to vibration of B-B bonds. Starting with the boron *Pmmm* system, we see that due to the specific atomic arrangements making up this two-sublayer material we have 12 Raman active modes. Among these, we only observe five Raman peaks (including two modes of in-plane displacements) with seven weak intensity peaks. The missing peaks are related to vibrations with small Raman tensor elements as shown in the SM [42]. For *Pmmn* boron, which also features a corrugated

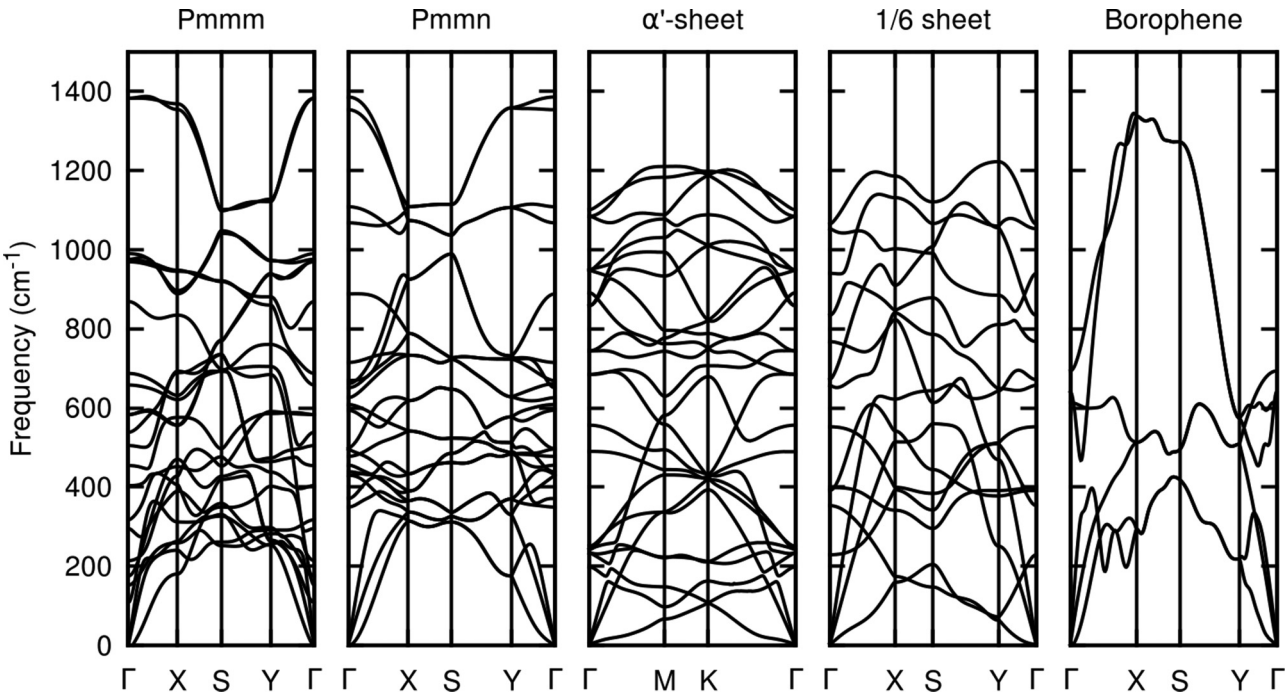

FIG. 2. Phonon dispersion curves for all materials considered in this study. The high symmetry points in the Brillouin zone are Γ (0,0,0), *X* (0.5,0,0), *S* (0.5,0.5,0), and *Y* (0,0.5,0). For the hexagonal system the points are *M* (0.5,0,0) and *K* (1/3,1/3,0).

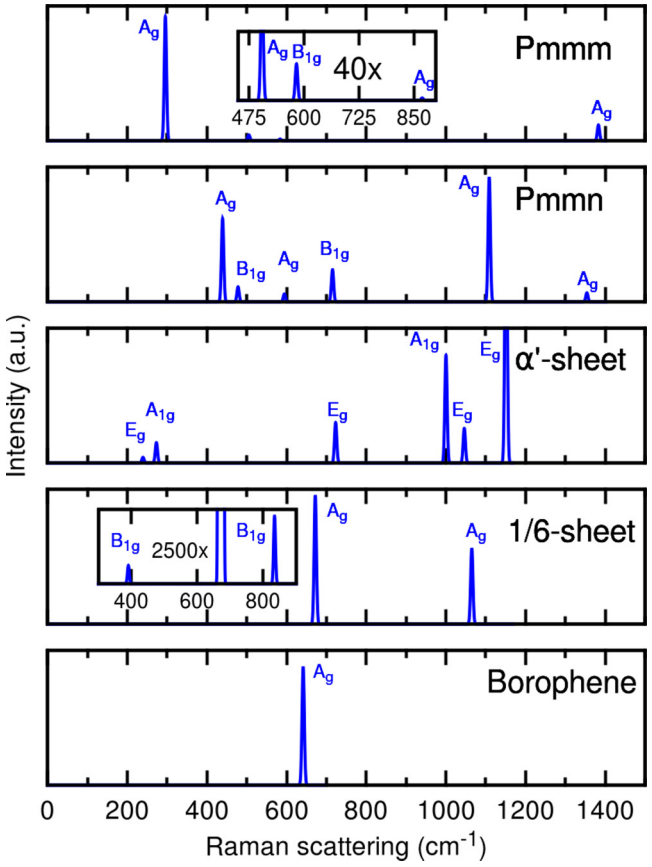

FIG. 3. Raman peak intensities, as obtained within density functional theory. The insets zoom on signal with weaker intensity. The vibrational patterns of these peaks can be seen in the SM [42].

surface, we calculated 12 active Raman modes. Only half of these provides nonvanishing Raman peak intensity with four in-plane displacement modes.

Moving to the Raman signature of flatter 2D boron sheets such the α'-sheet, 1/6-sheet, and borophene, we observe fewer Raman active modes due to the presence of a horizontal plane in the symmetry group of the respective systems. For instance, the α'-sheet presents 10 Raman active modes and four of them are doubly degenerated due to symmetry. The four high frequency modes correspond to in-plane motions. In contrast, the 1/6-sheet is perfectly flat and it shows six Raman active modes with four in-plane Raman peaks. The Raman intensity of two out-of-plane vibrations is very small due to negligible corresponding Raman tensor elements.

Finally, borophene has three active Raman modes and one Raman peak. In ascending order of frequency, the displacements are in the y, z, and x directions. One notable feature missing in this spectrum, compared to other boron materials, is the $\sim$1000 cm^{-1} Raman mode, related to the B-B bonding oscillations.

Finally we recall that our simulations only include first-order (i.e., one-phonon) Raman scattering, and it follows that only Γ-centered zone phonon modes are involved due to momentum conservation. However, multiphonon (typically two-phonon) processes involving phonons across the Brillouin zone can also occur and higher-frequency Raman peaks could

TABLE II. Calculated Raman active modes. Modes assigned with a w label have a weak signal, and a d annotation corresponds to a degenerate mode. Frequencies are expressed in cm^{-1}.

Pmmm						
Mode	B_{2g}	B_{3g}	B_{3g}	A_g	B_{2g}	A_g
Frequency	108.6^w	152.3^w	175.5^w	295.4	404.0^w	505.2
	B_{1g}	B_{3g}	A_g	B_{3g}	B_{2g}	A_g
	583.6	687.6^w	869.2	973.3^w	976.1^w	1383.2
Pmmn						
Mode	B_{2g}	A_g	B_{3g}	B_{1g}	B_{2g}	A_g
Frequency	430.3^w	439.1	455.6^w	477.9	496.4^w	594.3
	B_{3g}	B_{2g}	B_{1g}	B_{3g}	A_g	A_g
	609.2^w	669.6^w	715.3	888.6^w	1108.9	1354.2
α'-sheet						
Mode	E_g	A_{1g}	E_g	A_{1g}	E_g	E_g
Frequency	239.1^d	272.9	723.1^d	1000.2	1046.3^d	1151.1^d
1/6-sheet						
Mode	B_{3g}	B_{1g}	B_{3g}	A_g	B_{1g}	A_g
Frequency	229.1^w	391.4	552.7^w	671.9	834.4	1065.1
Borophene						
Mode	B_{3g}	A_g	B_{2g}			
Frequency	613.6^w	641.5	693.8^w			

appear, similar to the characteristic D and 2D peaks observed in graphene [45].

All systems, with the exception of α'-sheet, present in-plane anisotropic structure. Raman is very useful to access this information and has been recently applied in anisotropic phosphorene and ReS_2/$ReSe_2$ to identify the crystalline orientation in experiments [46–51]. Usually two methods are possible to measure polarization-dependence properties. One consists of rotating the sample with fixed polarization of incoming and scattered lights, and the other one is based on changing the polarization of the light while keeping the sample fixed. Analysis of the Raman tensors shows that only the A_g and B_{2g} modes can contribute to polarization effects. Specifically, in Appendix A, we show how the relative orientation of boron materials *Pmmm*, *Pmmn*, 1/6-sheet, and borophene can be determined using Raman polarization techniques.

C. Scanning tunneling microscopy signatures

The calculated Raman spectra indicate clear differences between the various 2D allotropes of boron considered, and it is expected to enable the experimental distinction among possible stable and metastable structures. In addition to Raman, other surface characterization techniques can be used to aid in the structural assignment. For instance, STM is a very powerful tool to interrogate the low-lying electronic structure of adsorbates. We note that while STM is often considered as a *topographic* analytical tool, it really offers only a snapshot of the electronic density integrated in the energy range between the energy corresponding to the applied tip bias and the Fermi energy. In other words an STM image does not always correspond directly to the topography (i.e., atomic positions) of the adsorbates, especially in low-dimensional systems where quantum confinement can yield integrated electronic density with symmetry that is often in clear departure from the

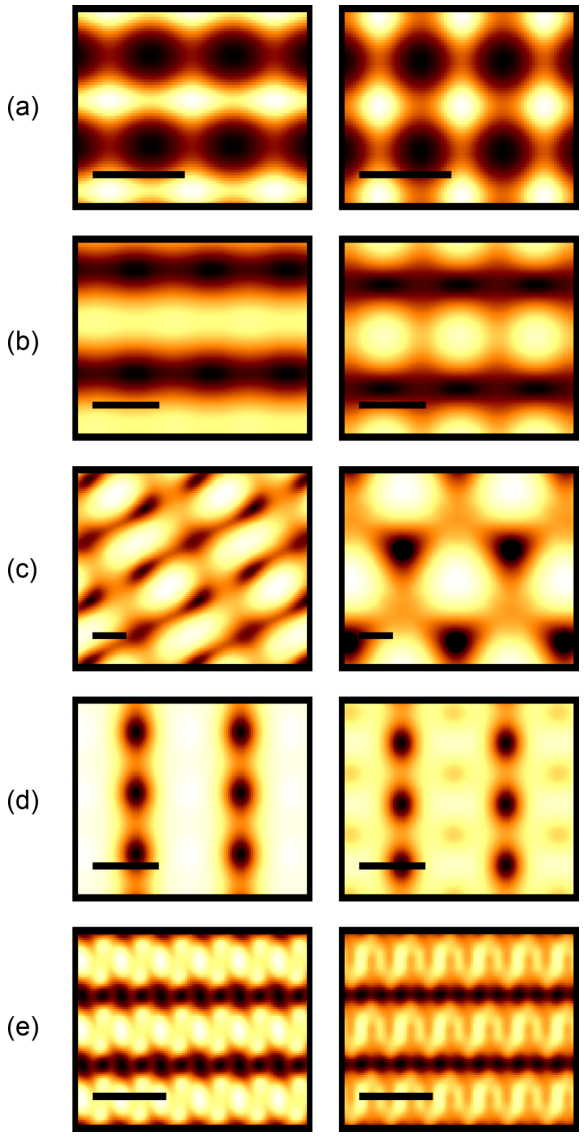

FIG. 4. Simulated STM images. Color map scale means tip height (Å) from 0.0 Å up to the number indicated in parenthesis for: (a) *Pmmm* (0.6 Å), (b) *Pmmn* (0.7 Å), (c) α'-sheet (0.8 Å), (d) 1/6-sheet (0.8 Å), and (e) borophene (0.03 Å). Black scale is 3 Å length.

full symmetry of the surface atoms. For this reason, it is particularly useful to use simulated STM images to assist in the interpretation of experimental images. This task is well suited to DFT-based studies since the knowledge of the electronic density as the central variable offers a straightforward handle to numerically simulate the STM images from first principles, within the Tersoff-Hamann approximation. We present characteristic images corresponding to bias potentials typically used in experiments in Fig. 4. It is understood that if a substrate was included, the interaction between both materials might change the symmetry of STM images. However, if this interaction is small the change can be negligible.

First, we note that every material shows a unique STM signature. Boron *Pmmm* and *Pmmn* feature a rectangular symmetry, and in both systems, the negative bias images reveal a pattern of stripes while the positive bias image presents a number of dotted features. The analyzed bias potentials are -0.4 and 0.2 V for *Pmmm* and -0.1 and 0.5 V for *Pmmn*. The only system with hexagonal symmetry, α'-sheet, shows in-plane-like orbitals for negative bias (-0.2 V) and a π-like orbital for the positive one (0.5 V). In the positive bias, the trigonal symmetry is clearly shown. Since α'-sheet is a semiconductor, we observed images only at higher energies. For the 1/6-sheet, we observe identical features for negative bias (-0.8 V), as for *Pmmm* and *Pmmn*, with bright stripes composed of hexagons separated by parallel lines of holes. For boron 1/6-sheet, the images we simulated are very similar to Feng *et al.* images [16]. For positive bias (0.6 V), the center of the hexagons presents a small depression that gets (relatively) darker when the bias potential increases. Analyzing borophene we obtain stripelike images with bias values comprised between -0.5 and 0.8 V. Even though our simulations do not include substrate interaction, they reproduce the experimentally observed stripe features. Comparing our optimized lattice values with substrate constrained materials, we measure 3.4% strain in the smaller lattice and 1% in the larger one. Taking that into account, we could calculate similar images as obtained by Mannix *et al.* [15].

IV. CONCLUSION

In conclusion, we carried out a systematic study of the intrinsic properties of a number of 2D boron allotropes in order to aid in their experimental identification and characterization. We show that nondestructive methods like Raman are able to fully discern the various phases of 2D Boron, even for phases with similar energetics. We listed all Raman active modes calculated by our methodology as a guide for experimental Raman characterization. We understand that the materials' community is debating whether or not some of the boron allotropes can be synthesized. We show that Raman spectroscopy could be one of the most important characterization techniques since we can identify unequivocally all the simulated materials, thus correctly identifying them. In addition, some materials present anisotropic features that could allow polarized Raman experiments to identify their crystalline orientation. Finally, STM images provide complementary insight on the local structural and electronic properties of boron materials. All in all, our study establishes that 2D B materials feature a large variety of electronic and vibrational properties, showing a rich physics that could lead to promising B-based applications.

ACKNOWLEDGMENTS

D.V.P.M. acknowledges CNPq-Brazil for financial support. The computations were performed using the resources of the Center for Computational Innovation at RPI. L.L. was supported by Eugene P. Wigner Fellowship at Oak Ridge National Laboratory and also acknowledges work at the Center for Nanophase Materials Sciences, a DOE Office of Science User Facility. N.K. was supported by the Office of Naval Research.

APPENDIX: RAMAN TENSORS, BACKSCATTERING AND POLARIZATION

Raman scattering is characterized by tensors, as provided by Eq. (2). For point group symmetry D_{2h}, the Raman active modes are characterized by the following tensors:

$$\tilde{\boldsymbol{R}}(A_g) = \begin{pmatrix} a & \cdot & \cdot \\ \cdot & b & \cdot \\ \cdot & \cdot & c \end{pmatrix} \tilde{\boldsymbol{R}}(B_{1g}) = \begin{pmatrix} \cdot & d & \cdot \\ d & \cdot & \cdot \\ \cdot & \cdot & \cdot \end{pmatrix}$$

$$\tilde{\boldsymbol{R}}(B_{2g}) = \begin{pmatrix} \cdot & \cdot & e \\ \cdot & \cdot & \cdot \\ e & \cdot & \cdot \end{pmatrix} \tilde{\boldsymbol{R}}(B_{3g}) = \begin{pmatrix} \cdot & \cdot & \cdot \\ \cdot & \cdot & f \\ \cdot & f & \cdot \end{pmatrix}.$$

The values corresponding to a–f are major terms while others (denoted by "·") are either zero or negligible due to symmetry. Four of the systems considered here possess the D_{2h} symmetry. The exception is the α'-sheet, which has a D_{3d} symmetry with tensors represented by

$$\tilde{\boldsymbol{R}}(A_{1g}) = \begin{pmatrix} g & \cdot & \cdot \\ \cdot & g & \cdot \\ \cdot & \cdot & h \end{pmatrix} \tilde{\boldsymbol{R}}(E_{g,1}) = \begin{pmatrix} i & \cdot & \cdot \\ \cdot & -i & j \\ \cdot & j & \cdot \end{pmatrix}$$

$$\tilde{\boldsymbol{R}}(E_{g,2}) = \begin{pmatrix} \cdot & -i & -j \\ -i & \cdot & \cdot \\ -j & \cdot & \cdot \end{pmatrix}.$$

Here, the nonzero elements correspond to values g–j. Experimentally, backscattering, where light propagates in the direction normal to the sample, is the most convenient setup. Thus, considering that the materials are oriented in the xy plane, the incoming and scattered lights are oriented along the z axis. For unpolarized light, the electric field is parallel to the surface of the material. A specific polarization corresponds to a well-defined angle θ between the x axis and the $\mathbf{g_i}$ vector. To emphasize the independence between incoming and scattered polarizations, $\mathbf{g_s}$ can have a polarization represented by another angle, α. With these notations, we have $\mathbf{g_i} = (\cos\theta, \sin\theta, 0)$ and $\mathbf{g_s} = (\cos\alpha, \sin\alpha, 0)$. From equation (1), the Raman intensity is given by $I \approx |\mathbf{g}_s \cdot \tilde{\boldsymbol{R}} \cdot \mathbf{g}_i^T|^2$.

We can calculate the intensity dependence for each mode using tensors for point group D_{2h} provided above. For A_g, the intensity is

$$I_{A_g} \approx a^2 |\cos\theta \cos\alpha + (b/a) \sin\theta \sin\alpha|^2, \tag{A1}$$

while for mode B_{1g} the calculated intensity is

$$I_{B_{1g}} \approx d^2 \sin^2(\alpha + \theta), \tag{A2}$$

which is only zero if the sum between polarization angles is 90°. In the backscattering configuration the modes B_{2g} and B_{3g} do not contribute to the Raman spectra.

Repeating the same analysis for point group D_{3d}, the intensity for A_{1g} mode is $I \approx g^2 |\cos\theta \cos\alpha + \sin\theta \sin\alpha|^2$, similar to the result obtained for the A_g of the D_{2h} group. For E_g modes, all elements are in x and y directions in the tensors, and when the intensities are added, we see that the corresponding intensity does not depend on the polarization angle [34].

Another information we can extract from Raman simulations is the crystalline orientation for the anisotropic crystals $Pmmm$, $Pmmn$, 1/6-sheet, and borophene. We will followi an approach similar to that employed in the work of Ling

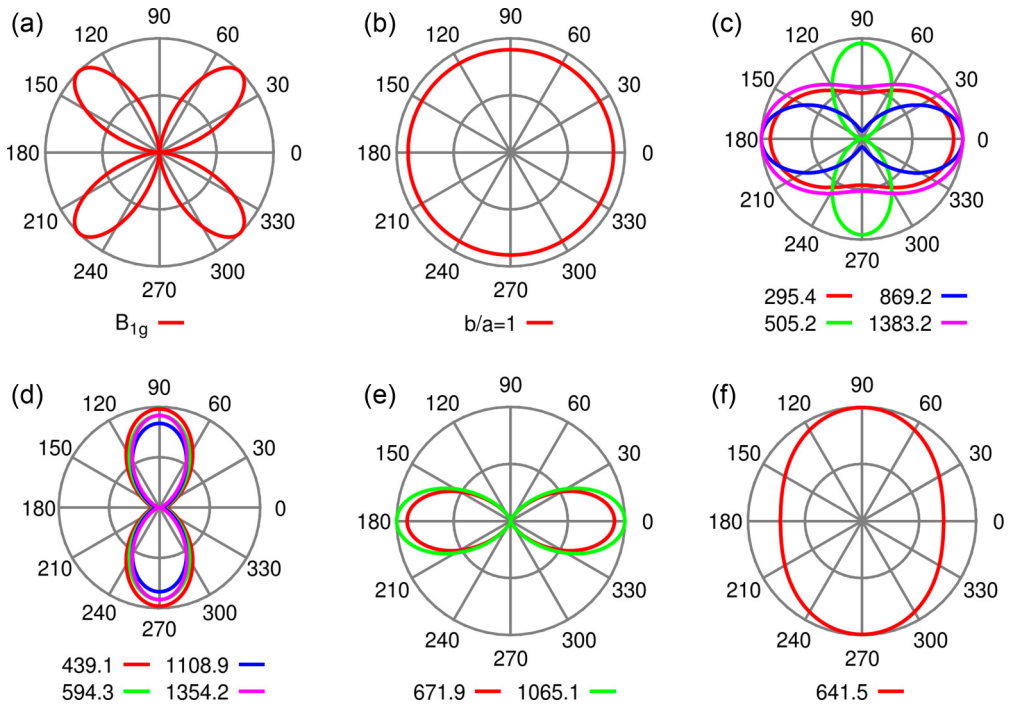

FIG. 5. Angular dependence of Raman intensity for materials with D_{2h} symmetry. The intensity is normalized for visualization, angles are expressed in degrees, and frequency values are given in cm^{-1}. (a) Polarization dependence for the B_{1g} modes. The polarization dependence for the A_g mode is shown in panels (b)–(f). Panel (b) represents the hypothetical case of isotropic material (i.e., $b/a = 1$). Plots are provided for (c) $Pmmm$, (d) $Pmmn$, (e) 1/6-sheet, and (f) borophene, with actual angle dependence provided by ratios collated in Table III.

et al. where the crystalline orientations for phosphorene were obtained by means of experiments and simulations of Raman polarized spectroscopy [46]. The in-plane rotation of the crystal by ϕ is equivalent to a rotation of both incoming and scattered light by $-\phi$ with the sample fixed. If we consider parallel polarization ($\theta = \alpha$) for point group D_{2h} and the polarization alignment with the x axis (which means $\theta = 0$), and then rotate the sample by ϕ, equations (A1) and (A2) become

$$I_{A_g} \approx a^2 |1 + (b/a - 1)\sin^2(\phi)|^2 \tag{A3}$$

and

$$I_{B_{1g}} \approx d^2 \sin^2(2\phi) \tag{A4}$$

after elementary manipulation.

The intensity of mode A_g depends on sample rotation angle ϕ and ratio b/a. For mode B_{1g} there is only angular dependence for the intensity. It reaches a minimum when $\phi = 0°, 90°, 180°$, and $270°$. It is maximum when $\phi = 45°, 135°, 225°$, and $315°$, as shown in Fig. 5(a).

For A_g mode, if $b/a = 1$, then the material would be isotropic, with a constant radial dependence [Fig. 5(b)]. However, for anisotropic materials, $b/a > 1$ or $b/a < 1$ and the periodicity is $180°$, with a position of the maximum and minimum intensity depending on the actual value of b/a. When $b/a > 1$, the maxima are locate in $\phi = 90°$ or $\phi = 270°$. The minima are rotated by $90°$, $\phi = 0°$, or $\phi = 180°$. The opposite is true for $b/a < 1$, as we can see in Fig. 5(c).

TABLE III. Ratio b/a for materials with point group D_{2h} symmetry calculated with the incident laser energy as 1.96 eV (633 nm). Frequencies of A_g modes are in cm^{-1}.

Pmmm				
Frequency	295.4	505.2	869.2	1383.2
Ratio	0.71	6.91	0.27	0.72
Pmmn				
Frequency	439.1	594.3	1108.9	1354.2
Ratio	3.57	4.28	4.84	13.53
1/6-sheet				
Frequency	671.9	1065.1		
Ratio	0.005	0.002		
Borophene				
Frequency	641.5			
Ratio	1.18			

When the ratio is $b/a > 1$, the maximum Raman intensity is aligned with the L_y lattice direction. Conversely, the minimum represents an alignment with L_x lattice direction. The opposite is true when $b/a < 1$. Table III provides the DFT-calculated b/a ratios for all A_g modes when the incident laser energy is 1.96 eV (633 nm). It is important to note that the calculated b/a ratios could change with respect to the laser energy, leading to different angular dependence for A_g modes, depending on the magnitude of b/a.

[1] K. S. Novoselov, A. K. Geim, S. V. Morozov, D. Jiang, Y. Zhang, S. V. Dubonos, I. V. Grigorieva, and A. A. Firsov, Science **306**, 666 (2004).

[2] G. R. Bhimanapati, Z. Lin, V. Meunier, Y. Jung, J. Cha, S. Das, D. Xiao, Y. Son, M. S. Strano, V. R. Cooper *et al.*, ACS Nano **9**, 11509 (2015).

[3] P. Vogt, P. De Padova, C. Quaresima, J. Avila, E. Frantzeskakis, M. C. Asensio, A. Resta, B. Ealet, and G. Le Lay, Phys. Rev. Lett. **108**, 155501 (2012).

[4] B. Aufray, A. Kara, S. Vizzini, H. Oughaddou, C. Leandri, B. Ealet, and G. Le Lay, Appl. Phys. Lett. **96**, 183102 (2010).

[5] A. Fleurence, R. Friedlein, T. Ozaki, H. Kawai, Y. Wang, and Y. Yamada-Takamura, Phys. Rev. Lett. **108**, 245501 (2012).

[6] L. Tao, E. Cinquanta, D. Chiappe, C. Grazianetti, M. Fanciulli, M. Dubey, A. Molle, and D. Akinwande, Nat. Nanotechnol. **10**, 227 (2015).

[7] E. Bianco, S. Butler, S. Jiang, O. D. Restrepo, W. Windl, and J. E. Goldberger, ACS Nano **7**, 4414 (2013).

[8] M. Dávila, L. Xian, S. Cahangirov, A. Rubio, and G. Le Lay, New J. Phys. **16**, 095002 (2014).

[9] S. Jiang, S. Butler, E. Bianco, O. D. Restrepo, W. Windl, and J. E. Goldberger, Nat. Commun. **5**, 3389 (2014).

[10] F.-f. Zhu, W.-j. Chen, Y. Xu, C.-l. Gao, D.-d. Guan, C.-h. Liu, D. Qian, S.-C. Zhang, and J.-f. Jia, Nat. Mater. **14**, 1020 (2015).

[11] W. Lu, H. Nan, J. Hong, Y. Chen, C. Zhu, Z. Liang, X. Ma, Z. Ni, C. Jin, and Z. Zhang, Nano Research **7**, 853 (2014).

[12] L. Li, Y. Yu, G. J. Ye, Q. Ge, X. Ou, H. Wu, D. Feng, X. H. Chen, and Y. Zhang, Nat. Nanotechnol. **9**, 372 (2014).

[13] H. Liu, A. T. Neal, Z. Zhu, Z. Luo, X. Xu, D. Tománek, and P. D. Ye, ACS Nano **8**, 4033 (2014).

[14] F. Xia, H. Wang, and Y. Jia, Nat. Commun. **5**, 4458 (2014).

[15] A. J. Mannix, X.-F. Zhou, B. Kiraly, J. D. Wood, D. Alducin, B. D. Myers, X. Liu, B. L. Fisher, U. Santiago, J. R. Guest, M. J. Yacaman, A. Ponce, A. R. Oganov, M. C. Hersam, and N. P. Guisinger, Science **350**, 1513 (2015).

[16] B. Feng, J. Zhang, Q. Zhong, W. Li, S. Li, H. Li, P. Cheng, S. Meng, L. Chen, and K. Wu, Nat. Chem. **8**, 563 (2016).

[17] B. Feng, J. Zhang, R.-Y. Liu, T. Iimori, C. Lian, H. Li, L. Chen, K. Wu, S. Meng, F. Komori, and I. Matsuda, Phys. Rev. B **94**, 041408 (2016).

[18] H. Tang and S. Ismail-Beigi, Phys. Rev. Lett. **99**, 115501 (2007).

[19] H. Tang and S. Ismail-Beigi, Phys. Rev. B **82**, 115412 (2010).

[20] X. Wu, J. Dai, Y. Zhao, Z. Zhuo, J. Yang, and X. C. Zeng, ACS Nano **6**, 7443 (2012).

[21] X.-F. Zhou, X. Dong, A. R. Oganov, Q. Zhu, Y. Tian, and H.-T. Wang, Phys. Rev. Lett. **112**, 085502 (2014).

[22] Z. Zhang, Y. Yang, G. Gao, and B. I. Yakobson, Angew. Chem., Int. Ed. **54**, 13022 (2015).

[23] S. De, A. Willand, M. Amsler, P. Pochet, L. Genovese, and S. Goedecker, Phys. Rev. Lett. **106**, 225502 (2011).

[24] W. Kohn and L. J. Sham, Phys. Rev. **140**, A1133 (1965).

[25] G. Kresse and J. Furthmüller, Phys. Rev. B **54**, 11169 (1996).

[26] G. Kresse and D. Joubert, Phys. Rev. B **59**, 1758 (1999).

[27] P. E. Blöchl, Phys. Rev. B **50**, 17953 (1994).

[28] J. P. Perdew, K. Burke, and M. Ernzerhof, Phys. Rev. Lett. **77**, 3865 (1996).

[29] J. P. Perdew, M. Ernzerhof, and K. Burke, J. Chem. Phys. **105**, 9982 (1996).
[30] J. Tersoff and D. R. Hamann, Phys. Rev. B **31**, 805 (1985).
[31] P. Umari, A. Pasquarello, and A. Dal Corso, Phys. Rev. B **63**, 094305 (2001).
[32] M. Ceriotti, F. Pietrucci, and M. Bernasconi, Phys. Rev. B **73**, 104304 (2006).
[33] K. Parlinski, Software PHONON, Poland (2010).
[34] L. Liang and V. Meunier, Nanoscale **6**, 5394 (2014).
[35] K. Parlinski, Z. Q. Li, and Y. Kawazoe, Phys. Rev. Lett. **78**, 4063 (1997).
[36] L. Liang, E. Cruz-Silva, E. C. Girão, and V. Meunier, Phys. Rev. B **86**, 115438 (2012).
[37] L. Liang and V. Meunier, Appl. Phys. Lett. **102**, 143101 (2013).
[38] M. Profeta and F. Mauri, Phys. Rev. B **63**, 245415 (2001).
[39] E. del Corro, A. Botello-Mndez, Y. Gillet, A. L. Elias, H. Terrones, S. Feng, C. Fantini, D. Rhodes, N. Pradhan, L. Balicas, X. Gonze, J.-C. Charlier, M. Terrones, and M. A. Pimenta, Nano Lett. **16**, 2363 (2016).
[40] C. Van Caillie and R. D. Amos, Phys. Chem. Chem. Phys. **2**, 2123 (2000).
[41] E. T. Heyen, S. N. Rashkeev, I. I. Mazin, O. K. Andersen, R. Liu, M. Cardona, and O. Jepsen, Phys. Rev. Lett. **65**, 3048 (1990).
[42] See Supplemental Material at http://link.aps.org/supplemental/10.1103/PhysRevB.94.195416 for structural properties, band-structure and vibrational modes for 2D boron materials.
[43] Z. Zhang, A. J. Mannix, Z. Hu, B. Kiraly, N. P. Guisinger, M. C. Hersam, and B. I. Yakobson, Nano Letters **16**, 6622 (2016).
[44] P. Giannozzi, S. Baroni, N. Bonini, M. Calandra, R. Car, C. Cavazzoni, D. Ceresoli, G. L. Chiarotti, M. Cococcioni, I. Dabo, A. D. Corso, S. de Gironcoli, S. Fabris, G. Fratesi, R. Gebauer, U. Gerstmann, C. Gougoussis, A. Kokalj, M. Lazzeri, L. Martin-Samos, N. Marzari, F. Mauri, R. Mazzarello, S. Paolini, A. Pasquarello, L. Paulatto, C. Sbraccia, S. Scandolo, G. Sclauzero, A. P. Seitsonen, A. Smogunov, P. Umari, and R. M. Wentzcovitch, J. Phys.: Condens. Matter **21**, 395502 (2009).
[45] A. C. Ferrari and D. M. Basko, Nat. Nano **8**, 235 (2013).
[46] X. Ling, L. Liang, S. Huang, A. A. Puretzky, D. B. Geohegan, B. G. Sumpter, J. Kong, V. Meunier, and M. S. Dresselhaus, Nano Lett. **15**, 4080 (2015).
[47] J. Wu, N. Mao, L. Xie, H. Xu, and J. Zhang, Angew. Chem. **127**, 2396 (2015).
[48] H. B. Ribeiro, M. A. Pimenta, C. J. S. de Matos, R. L. Moreira, A. S. Rodin, J. D. Zapata, E. A. T. de Souza, and A. H. C. Neto, ACS Nano **9**, 4270 (2015).
[49] H. Zhao, J. Wu, H. Zhong, Q. Guo, X. Wang, F. Xia, L. Yang, P. Tan, and H. Wang, Nano Research **8**, 3651 (2015).
[50] D. Wolverson, S. Crampin, A. S. Kazemi, A. Ilie, and S. J. Bending, ACS Nano **8**, 11154 (2014).
[51] D. A. Chenet, O. B. Aslan, P. Y. Huang, C. Fan, A. M. van der Zande, T. F. Heinz, and J. C. Hone, Nano Lett. **15**, 5667 (2015).